Laser Guide Star Return Flux Simulations Based on Observed Sodium Density Profiles

Ronald Holzlöhner[1], Simon M. Rochester[2], Thomas Pfrommer[3], Domenico Bonaccini Calia[1], Dmitry Budker[2], James M. Higbie[4], and Wolfgang Hackenberg[1]

[1] Laser Systems Department, European Southern Observatory (ESO), Karl-Schwarzschild-Str. 2, D-85748 Garching b. München, Germany, http://www.eso.org/sci/facilities/develop/lgsf/

[2] University of California Berkeley, Department of Physics, Berkeley, CA 94720-7300, USA

[3] Department of Physics and Astronomy, University of British Columbia, Vancouver, British Columbia, Canada

[4] Bucknell University, Department of Physics, 701 Moore Avenue, Lewisburg, PA 17837, USA

ABSTRACT

We extend previous sodium LGS models by integrating the return flux across the mesosphere, taking into account variable mesospheric gas density, temperature, and local sodium density. This method allows us to produce accurate predictions of the actual return flux on the ground, relevant for determining the performance of adaptive-optics-assisted instruments. We find that the flux distribution across the sky depends strongly on geographic location and laser parameters. Almost independent of location, future sodium LGS will be about three times brighter at zenith than at the observing horizon.

Keywords: Laser guide stars, Atmospheric propagation, Laser beam transmission, Wavefront sensing

1. INTRODUCTION

The upcoming generation of 30+m telescopes will rely for their operation on sodium laser guide star (LGS) assisted adaptive optics (AO). Because powerful lasers at 589 nm are difficult to produce and expensive, the required laser power and format to achieve the return flux specifications must be accurately modeled. Previous simulations describe the efficiency of cw LGS lasers [1], but are based on numerous assumptions and simplifications, regarding specifically the mesospheric sodium distribution, mesospheric temperature, and gas densities.

The return flux from sodium LGS depends on, among various other parameters, atomic collision rates and mesospheric temperatures. Moreover, the photon return flux per atom is in general a nonlinear function of laser irradiance In order to accurately compute the cw LGS return flux for a given parameter set, one needs to integrate the return signal along the laser beam in the mesosphere for each pointing direction on the sky.

In our previous Bloch simulations [1], we assumed `hard collisions' that completely reset the atomic velocity of sodium with no memory of the initial velocity. In reality, `soft collisions' at grazing incidence that only alter the velocity vectors slightly occur much more frequently. The consequence is an intensified local diffusion in velocity space, i.e., atoms leap rapidly among neighboring velocity classes, but less often incur large velocity changes. The results in this work are based on a more accurate, modified algorithm that takes the physics of soft collisions, corresponding to realistic differential cross sections, into account. We will describe the details of the algorithm elsewhere.

2. MODELING SETUP

2.1 Return flux integral

Starting from Eqs. (4),(5) of [1], we define the quantity

$$\kappa(I) = I \frac{dA}{dI}; \quad \text{with} \quad P_{\text{meso}} = \frac{P_{\text{launch}} \left(T_a \right)^X}{P_0} \int_0^{I_{\max}} \kappa(I) \, dI \,, \tag{1}$$

where I is mesospheric spot irradiance in W/m^2, dA/dI is the distribution function of I over the mesospheric area A orthogonal to the beam at some altitude when launching $P_0 = 1$ W of laser power, P_{launch} is the actual launched laser power, P_{meso} is the integrated mesospheric laser spot power, T_a is the atmospheric single-pass transmission at 589 nm and at zenith, and $X \approx \sec(\zeta)$ is the airmass at zenith angle ζ. The value of P_{meso} is in practice slightly smaller than 1 W due to diffraction at hard-edged apertures in the launch telescope, high spatial frequency scattering due to dust and/or micro-grooving on (in particularly large) optical surfaces caused by some manufacturing processes, scratches on optical surfaces, and small-scale atmospheric turbulence.

In the following, the symbol H denotes altitude above sea level, and $L = XH$ means distance from sea level to a point in the mesosphere along the laser beam direction. The irradiance histogram $\kappa(I)$ can be computed using physical optics simulations [2] and depends on the seeing [3], the outer turbulence scale, the launch telescope aperture, beam clipping, and the propagation distance $L_0 - XH_{\text{tele}}$ from the launch telescope to a given point L_0 in the mesosphere, where H_{tele} is the telescope altitude above sea level. We now approximate κ at any L by introducing the area scaling factor $s(L)$ based on the beam divergence in the mesosphere, where $s(L_0) = 1$. The mesospheric power integral can then be conceptually rewritten as

$$P_{\text{meso}} = \int_0^{I_{\text{max}}} \left(\frac{P_{\text{launch}} \left(T_a\right)^X I}{P_0 s(L)} \right) \left(\frac{s(L)\kappa(I)}{I} \right) dI \ . \tag{2}$$

The first fraction in the integrand (unit W/m^2) can be interpreted as the laser photon flux density at a specific altitude, and the second term is the area scaled irradiance distribution function. The return flux increment $d\Phi$ on the ground (in ph/s/m^2) that is produced at the distance L within the slice dL can be computed as

$$d\Phi = dL \left(T_a\right)^X \frac{d_{\text{Na}}\left(L/X\right)}{\left(L - XH_{\text{tele}}\right)^2} \int_0^{I_{\text{max}}} \psi \left(\frac{P_{\text{launch}} \left(T_a\right)^X I}{P_0 s(L)}, \theta, \frac{L}{X} \right) s(L)\kappa(I) \ dI \ , \tag{3}$$

where $\psi(I,\theta,H) = \Psi/I$ is the photon return flux per atom Ψ normalized by irradiance as defined in [1, Section 3.3], evaluated at irradiance I, the angle between beam and geomagnetic field lines θ, and at altitude H. We have also introduced the sodium atom number density per volume $d_{\text{Na}}(H)$ with

$$C_{\text{Na}} = \int_{H_{\text{min}}}^{H_{\text{max}}} d_{\text{Na}}(H) \ dH \ , \tag{4}$$

where C_{Na} is the sodium column density, and the limits H_{min} and H_{max} represent the vertical extent of the sodium column, namely the altitude range outside of which d_{Na} is negligible. The total LGS return photon flux on the ground, as defined by Eq.(6) of [1], can then be computed as the double integral

$$\Phi(\zeta,\theta) = \left(T_a\right)^X \int_{XH_{\text{min}}}^{XH_{\text{max}}} \frac{\eta(L)s(L)d_{\text{Na}}\left(L/X\right)}{\left(L - XH_{\text{tele}}\right)^2} \int_0^{I_{\text{max}}} \psi \left(\frac{\eta(L)P_{\text{launch}} \left(T_a\right)^X I}{P_0 s(L)}, \theta, \frac{L}{X} \right) \kappa(I) \ dI \ dL \ . \tag{5}$$

The inner integral over I yields the quantity F_m in [1, Eq.(6)]. In Eq.(5), we have additionally introduced the mesospheric light depletion function

$$\eta(L) = \exp\left(-\sigma_{\text{Na,eff}} \int_{XH_{\text{min}}}^{XH_{\text{max}}} d_{\text{Na}}(L) \ dL \right), \tag{6}$$

which equals the fraction of the remaining laser power at L due to sodium excitation, where $\sigma_{\text{Na,eff}}$ is the effective optical cross section of sodium at 589 nm for the typical beam irradiance ($\sigma_{\text{Na,eff}} \approx 0.85 \times 10^{-11}$ cm^2, see [1, Fig.1]). Equation (6) is the solution to the differential equation $d\eta/dL = -\sigma_{\text{Na,eff}} \eta d_{\text{Na}}(L)$. Since light depletion occurs on the downlink as well as on the uplink, we apply it twice in the calculation of Φ. Note that depletion is most severe at high altitude and airmass (up to about 4% depletion per pass at median sodium abundance), and it effectively exacerbates the atmospheric attenuation. Note also that Φ is not strictly proportional to C_{Na} anymore once we consider a nonzero η.

We are now ready to calculate the return flux $\Phi(\zeta,\theta)$, using the geometric formula (distance on unit sphere)

$$\theta = \arccos\left[\cos(\theta_L)\cos(\theta_B) + \cos(\varphi_L - \varphi_B)\sin(\theta_L)\sin(\theta_B)\right], \tag{7}$$

where θ_L and θ_B are the polar angles of the laser beam and the *B*-field in some local coordinate system, respectively, and φ_L and φ_B are the corresponding azimuths. In order to account for the finite radius of the Earth of $R = 6378$ km, we employ the corrected airmass formula

$$X(\varsigma) = -r\cos\varsigma + \sqrt{r^2\cos^2\varsigma + 2r + 1} \quad , \qquad r = \frac{R + H_{\text{tele}}}{H - H_{\text{tele}}} \; , \tag{8}$$

which becomes significant when pointing the laser close to the horizon ($\zeta > 50°$).

We note that we do not take into account atmospheric depolarization, which, however, was found to be a very small effect [4].

2.2 Data Input

We use the following three input data sets:
   a) MSISE-90 mesospheric gas density and temperature table from http://ccmc.gsfc.nasa.gov/modelweb/, (depends on altitude, season and year),
   b) Sodium profiles $d_{\text{Na}}(H)$ measured with the Large Zenith Telescope (LZT) LIDAR near Vancouver, CA [5], which we apply at any telescope location,
   c) Irradiance histogram at 1 W launched power from physical optics simulations [2] (depends on laser characteristics and the magnitude of *B*, launch equipment, seeing, outer turbulence scale, and the turbulence profile).

While the seasonal sodium abundance depends on the latitude [6,8], we believe that the set of sodium profiles measured near Vancouver can be taken as a representative sample set.

We then compute a table of $\psi(I,\theta,H)$ using the Bloch simulation with inputs of data table a) (depends on laser characteristics, atomic physics constants such as collision cross sections, and the magnitude of *B*). The data tables a)–c) and the table of $\psi(I,\theta,H)$ are then interpolated and the double integral in Eq.(5) is carried out numerically in a Mathematica routine.

Figure 1 shows an example of a simulated scaled irradiance histogram $\kappa(I)$ for a nominal 40 cm launch telescope (36 cm clear aperture) and 1 W launched laser power at 0.8" seeing (at 500 nm and zenith), $\zeta = 30°$, and 92 km altitude, corresponding to 103.9 km propagation distance (blue curve). A Gaussian irradiance profile, which one would obtain in the absence of turbulence and launch telescope aberrations, corresponds, by contrast, to $\kappa(I) = A_{\text{Gauss}} = A_{\text{eff}}/2$ up to $I = 2I_{P/2}$ and $\kappa(I) = 0$ for $I > 2I_{P/2}$, as shown by the green box. The quantity $I_{P/2}$ is the "50% power in the bucket irradiance" defined in [1, Eq.(5)], and satisfies $A_{\text{eff}} = P_{\text{meso}}/I_{P/2}$. Since the blue curve both has a long tail and seems to diverge at small irradiance, we can infer that the turbulence causes both high irradiance spikes due to small speckles and an extended pedestal ("blueberry sprinkled pancake"). The area under the blue curve and the area of the boxes all equal 1 W. The area scaling function is $s(L) = [\text{fwhm}(L{-}X\,H_{\text{tele}})/\text{fwhm}(L_0{-}X\,H_{\text{tele}})]^2$, where fwhm $= [2\log(2)A_{\text{eff}}/\pi]^{1/2}$ denotes the equivalent full width at half maximum beam profile diameter in the mesosphere. We find the fit function $\text{fwhm}(L) = 4.103\times10^{-6}\,L - 0.03568$, where lengths are in meters and $L_0{-}X\,H_{\text{tele}}$ = 103.9 km.
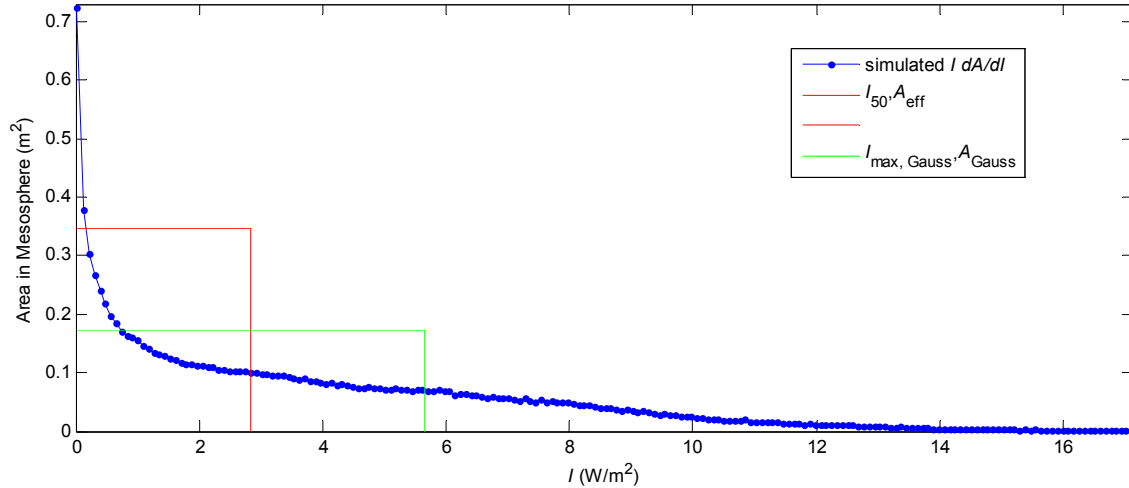
Fig.1: Blue curve: Scaled irradiance histogram $\kappa(I) = I\, dA/dI$ for a nominal 40 cm launch telescope and a 1 W laser at $\zeta = 30°$. Green box: $\kappa(I)$, red box: $I_{50} = I_{P/2}$ and A_{eff} for corresponding Gaussian beam.

The left plot of Fig. 2 shows the modeled number densities of N_2, O_2, and O, in Paranal for March 21, 2007 from MSISE-90 across the mesosphere. All densities vary by more than an order of magnitude across the 20 km height of the sodium layer. The right plot shows the mesospheric temperature distribution for January 15 (southern summer, minimum monthly average column abundance at 23°S of $3.5\times10^{13}/m^2$ according to Moussaoui et al. [6, Fig.16]), March 21 (default for all further simulations), June 21, and August 15 (maximum monthly average column abundance of $8.5\times10^{13}/m^2$ at 23°S). The temperature at 93–100 km altitude is actually the lowest in the entire atmosphere. The minimum January temperature at 97.5 km of 186 K is the highest of all four curves, agreeing with the seasonal temperature trend on the ground in the southern hemisphere.
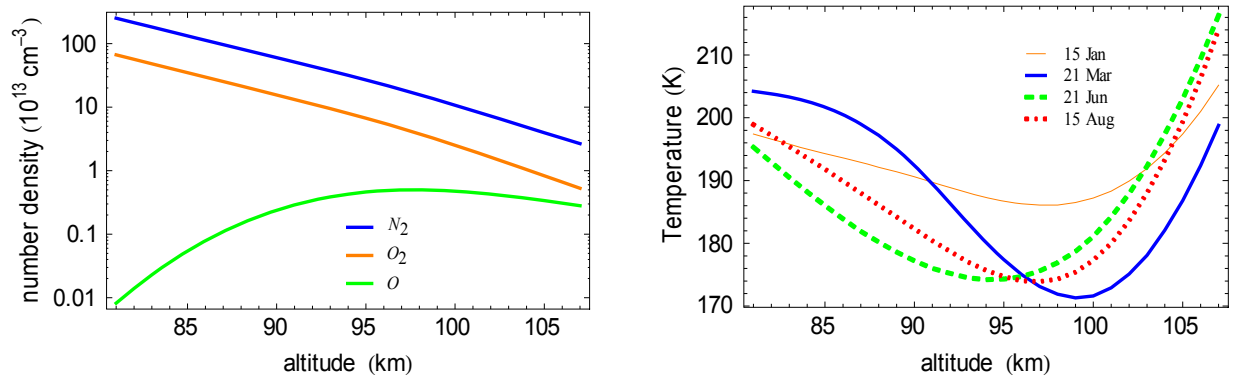
Fig.2: Left: Gas number densities of N_2, O_2, and O across the mesosphere. Note the logarithmic scale. Right: temperature.

Figure 3 displays four different sodium density profiles $d_{Na}(H)$ recorded at the LZT in 2008. Note that most profiles tend to have a sudden onset near 83 km altitude, but taper off more slowly above 95–105 km. We have smoothed and normalized the profiles for equal column densities in order to facilitate their comparison. The blue curve for July 8, 2008 is the default in all simulations discussed below.
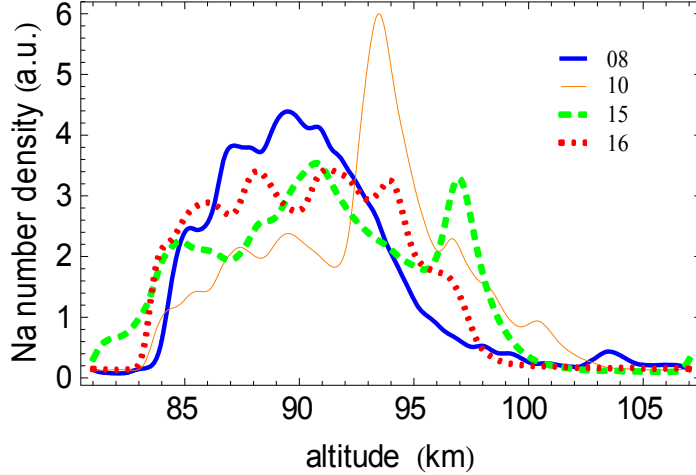
Fig.3: Normalized sodium density profiles d_{Na} taken during four nights in July 2008 at the LZT (day of month in legend).

3. RESULTS AND DISCUSSION

3.1 Sky Plots of Return Flux

We can now produce polar sky plots of Φ in the coordinates ($r = \cos(\zeta), \phi$). We first compare with measurements conducted in 2006 at the Starfire Optical Range (SOR, located at 35°N, 160°W [7]) and simulate their single-frequency 30 W `Fasor' laser with circular polarization and without repumping. There is no independent measurement of the sodium column density available, but Xiong and Gardner find $C_{Na} = 2\ldots10\times10^{13}/m^2$ at the SOR over the year [8, Fig1a], and Drummond reports $C_{Na} = 2\ldots12\times10^{13}/m^2$ [7, Fig.3], with spikes up to $C_{Na} = 20\times10^{13}/m^2$.

The left plot in Fig. 4 shows a comparison of measured return flux and simulation for SOR for a scan along the South–North meridian. Negative zenith angles denote southern orientation in this plot. The red dots depict Φ on October 23, 2006, with 30W of laser power [9, Fig.8a], of which we assume $P_{launch} = 0.95\times30\,W = 28.5\,W$ were launched into air. The solid line is our corresponding simulation result modeling the local SOR conditions, and we apply the fit parameters $T_a = 0.84$ and $C_{Na} = 20\times10^{13}/m^2$. The magnetic field lines at SOR point at an azimuth of $\varphi_L = 189°$ (South-South-West) and $\zeta = -62°$. The detrimental effect of Larmor rotation on Φ is zero in this direction, but since there is a competition with atmospheric attenuation at large ζ, $\Phi(\zeta)$ peaks at a much smaller zenith angle near $\zeta = -25°$. The agreement between experiment and simulation is good, although the experimental uncertainty is quite large. It is well known [6] that C_{Na} can vary rapidly both spatially and temporally during a night and even during an observation run, often by a factor of 2 or more, making quantitative comparisons challenging.

The sodium column density on October 23, 2006 was exceptionally high, possibly caused by a meteor shower. In Fig. 4, right, we show a sky plot of Φ at SOR for $C_{Na} = 5.8\times10^{13}/m^2$ that is closer to the median value. The South-North meridian is indicated by the vertical gray line. Note that Φ decays quickly when pointing the laser away from the magnetic field lines.
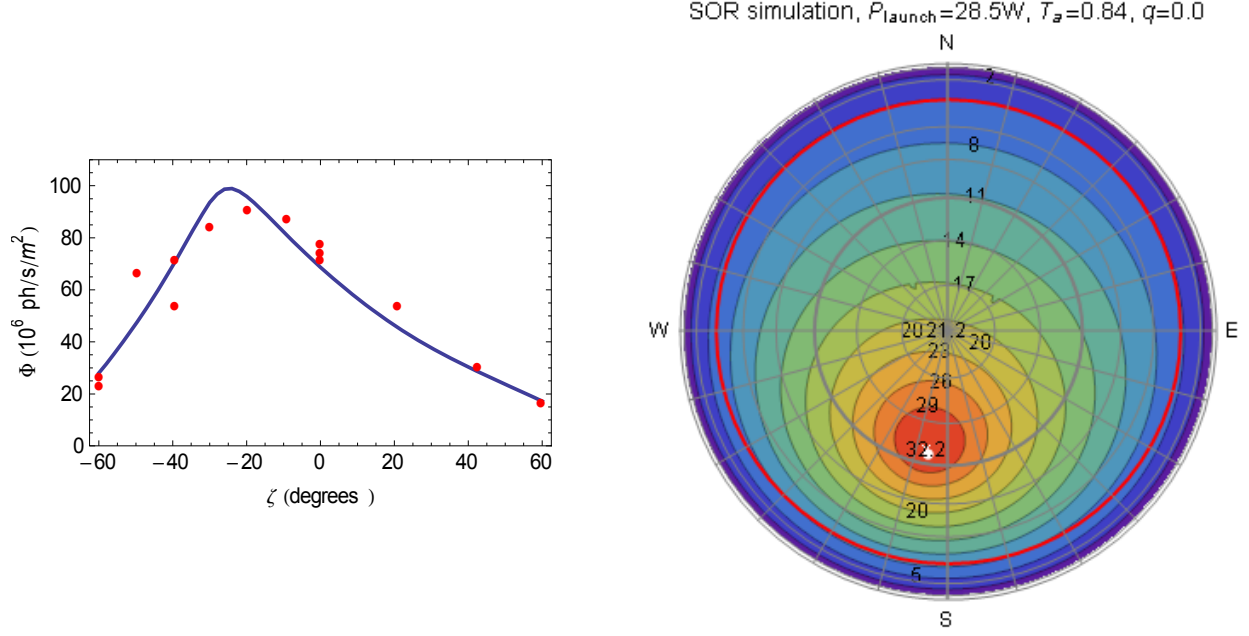
Fig.4: Left: Red dots: measured ground return flux Φ from Fasor at SOR for $P_{launch} = 28.5$ W without repumping ($q = 0$) along the South–North meridian, solid line: numerical simulation. Right: Sky plot of simulated Φ in 10^6 ph/s/m^2 (white dot: direction of magnetic field lines, red circle: $\zeta = 60°$ zenith angle = observing horizon).

Next, we simulate Φ for Cerro Paranal/Armazones and a 20 W laser of which 16 W are launched, with circular polarization (ESO Adaptive Optics Facility specifications) and single frequency (< 1 MHz). The strength of the geomagnetic field in Paranal is $B = 0.23$ G. Figure 5 shows corresponding sky plots with 12% repumping (left) and without repumping (right). Note that the number of contour lines was increased relative to Fig. 4 to display more detail. With repumping, we find $\Phi = 12.1 \times 10^6$ ph/s/m^2 on the ground from zenith with $C_{Na} = 4.0 \times 10^{13}$/m^2 and $T_a = 0.84$, meeting the draft E-ELT flux requirement of $\Phi = 10.3 \times 10^6$ ph/s/m^2 on the ground ($\Phi = 5 \times 10^6$ ph/s/m^2 at Nasmyth at zenith and $T_a = 0.89$ with a telescope transmission of 48.5%). The white cross indicates the direction of maximum return flux. In the absence of repumping, there is a significantly higher penalty for pointing at an angle to the magnetic field lines (white dot). We will therefore further only consider the case of circular polarization and 12% repumping.

The return flux optimum is generally tilted towards the South (North) in the northern (southern) hemisphere, which is beneficial for astronomy since the stars culminate on the meridian passing through the zenith and the poles in the direction towards South (North)". A less fortunate circumstance for observations is the rapid decay of Φ with the zenith angle, which amounts to approximately a factor of 3 from $\zeta = 0°$ to $60°$ ($X \approx 2$). This decay has four different reasons (we exclude the magnetic field effect for the moment):

1. The L^{-2} dependence of the solid angle that the detector subtends, as seen from the guide star. This effect is partly compensated by the apparent thickness variation of the sodium layer, scaling like X,
2. The double-pass atmospheric transmission in the line of sight that scales like $(T_a)^{2X}$,
3. Light depletion increase with ζ,
4. Spot size increase in the mesosphere with ζ, which influences (usually lowers) the sodium pumping efficiency.

From the first two geometric effects alone, one obtains the relationship

$$\frac{\Phi(X_2)}{\Phi(X_1)} = \frac{X_1 (T_a)^{2X_2}}{X_2 (T_a)^{2X_1}} , \qquad (9)$$

leading to a flux reduction of 1/2.8…1/2.5 when moving from $\zeta = 0°$ to 60° at $T_a = 0.84…0.89$. The single-pass light depletion η increases from 1.9% to 3.8% for Paranal conditions at $C_{Na} = 4.0×10^{13}/m^2$ at the same time (item 3). Finally, the reduction in Φ due to item 4 is about 7% for a diffraction-limited beam. Combined, Φ decays by over a factor of 3, which must be taken into account when modeling the performance of AO instrumentation. We add that the minimum flux at $\zeta = 60°$ of $Φ ≈ 3.3×10^6$ ph/s/m² in Paranal does not occur towards the South, but at $\varphi_L ≈ 105°$ and 255° (see Fig.5 left).

When an LGS system is actually employed as a LIDAR system (pulsed or CW) to study mesospheric sodium, the usual assumption is that the return flux from a given altitude is proportional to the local sodium density after correcting for geometric effects. In this context, we note that the spot size effect on Φ of item 4 above implies that the beams of 20W-class LGS lasers need to be defocused when run as a LIDAR to accurately measure sodium profiles.

We have also produced similar sky plots for the other sodium profiles and gas density/temperature profiles shown in Fig. 2 and Fig. 3 and found that Φ differs at zenith by less than one percent among those plots.
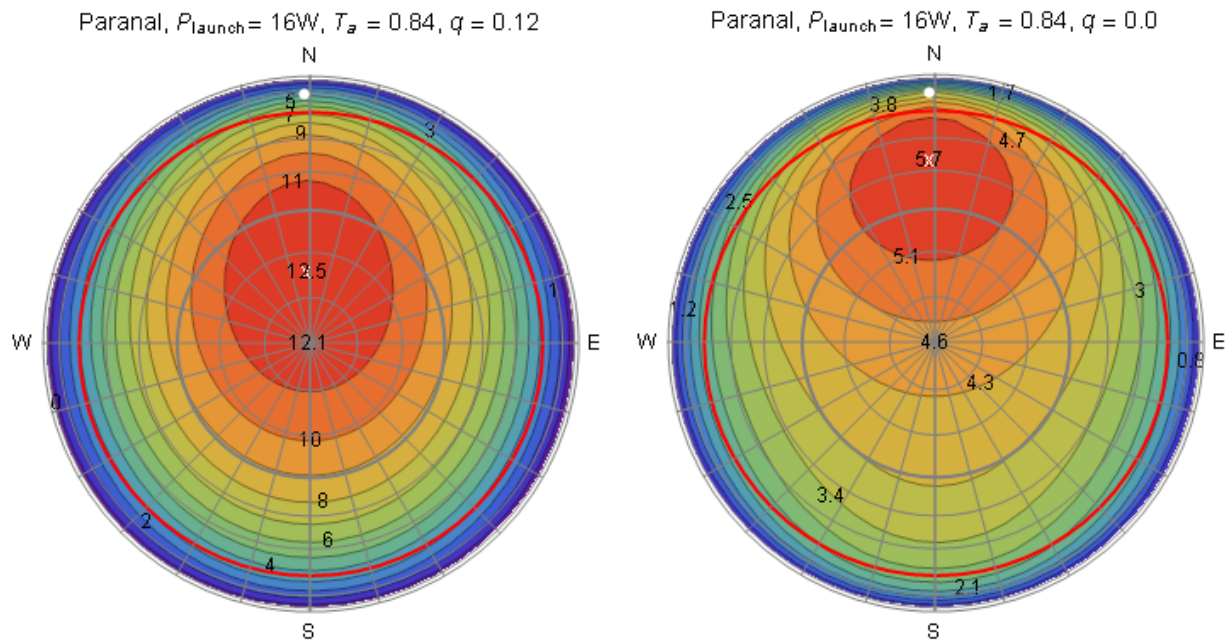
Fig.5: Sky plots of Φ in 10^6 ph/s/m² for Paranal for a 16 W in air with D_{2b} repumping (left, q = 12%), and without repumping (right, q = 0). White dot: direction of magnetic field lines, white cross: point of peak return, red circle: 60° zenith angle.

Earlier work of our group [10, Fig.13b] found that the peak return flux for Paranal lies further from zenith than our simulation in Fig. 5, while the situation for SOR is opposite [7, Fig. 13a]. The reason is probably that SOR's laser experiment did not include repumping, causing the return flux to decay faster as a function of θ, which is not taken into account in [10]. Repumping of $q ≈ 12\%$, on the other hand, helps to mitigate this deterioration; hence the return appears to be more exclusively governed by atmospheric attenuation. See also [1, Fig. 3].

Figure 6, left, shows Φ in Paranal when launching 0.8 × 30 W = 24 W instead of 16 W. The zenith return flux grows to $Φ = 17.8×10^6$ ph/s/m², while the linear scaling predicts 12.1×24/16 = 18.2 ph/s/m², indicating a gentle saturation of 2%. If the laser power is increased further, the laser bandwidth should be scaled proportionally in order to mitigate saturation. Figure 6, right, shows a simulation for 360 W at a laser FWHM bandwidth of 50 MHz (Lorentzian line shape). Since the natural width of the sodium D_2 line is about 10 MHz, one can conceptually consider more than five velocity classes to be excited, which significantly extends the pool of sodium atoms that can participate in the resonance fluorescence and thus
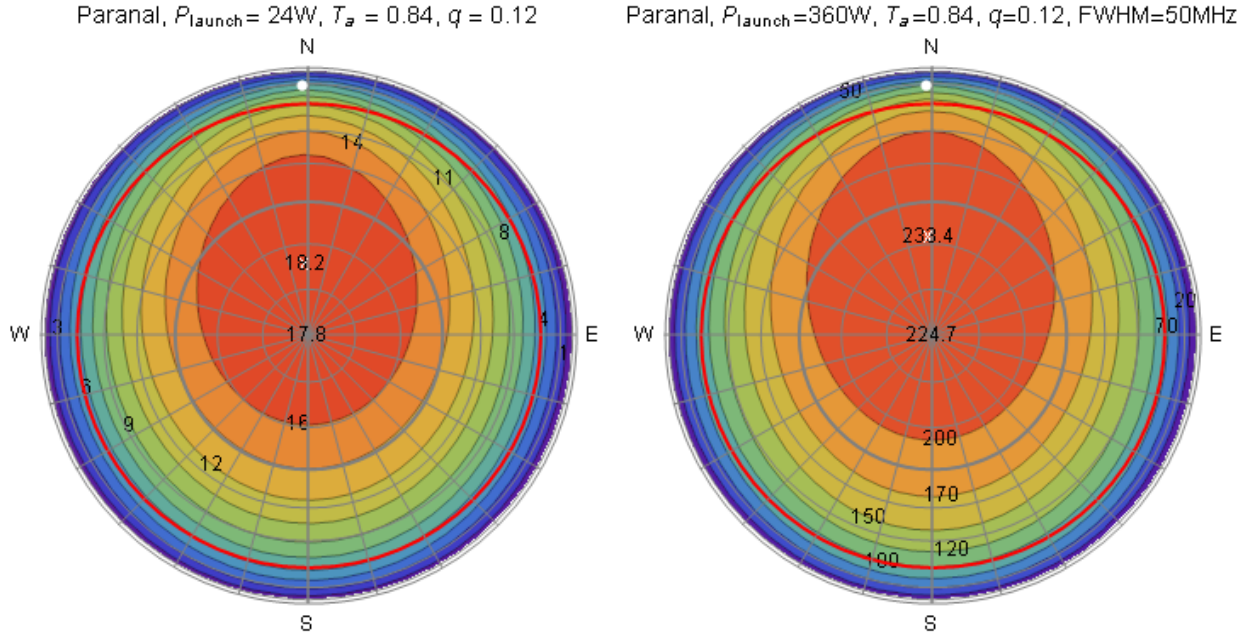
Fig. 6: Sky plots of Φ in 10^6 ph/s/m^2 for Paranal with repumping. Left: same as Fig.5 left but with 24 W in air, Right: with 360 W in air and 50 MHz laser linewidth

mitigates saturation. We achieve 224.7×10^6 ph/s/m^2 at zenith, which is 84% of the scaled 24 W flux of 17.8×10^6 ph/s/m$^2 \times 360$W/24W = 267×10^6 ph/s/m^2, while at single frequency, we would obtain only 59% (plot not shown). This result is relevant when designing pulsed LGS lasers for spot tracking (~3µs pulse duration) whose peak powers may be close to 400 W.

Finally, Fig. 7 portrays Φ for Mauna Kea, Hawaii (left, B=0.35), and for Mount Wendelstein, Southern Germany (right, B=0.46), with the same laser and beam parameters as in Fig. 5, left. The zenith return flux on Mauna Kea of $\Phi = 14 \times 10^6$ ph/s/m^2 is similar to that in Paranal. The observatory on the summit of Mount Wendelstein, located at 47.7°N, 12.0°E, close to ESO's headquarters in Garching, is a possible location for testing the transportable LGS projector that is under development at ESO at the moment (see paper 7736-65 in these proceedings). Obviously, the more vertical the magnetic field lines are pointing, the stronger Φ will peak near zenith. Additionally, the minimum return at $\zeta = 60°$ in the direction opposite of the field line pointing (close to due North in Fig. 6) is less diminished compared to the zenith return in this case.
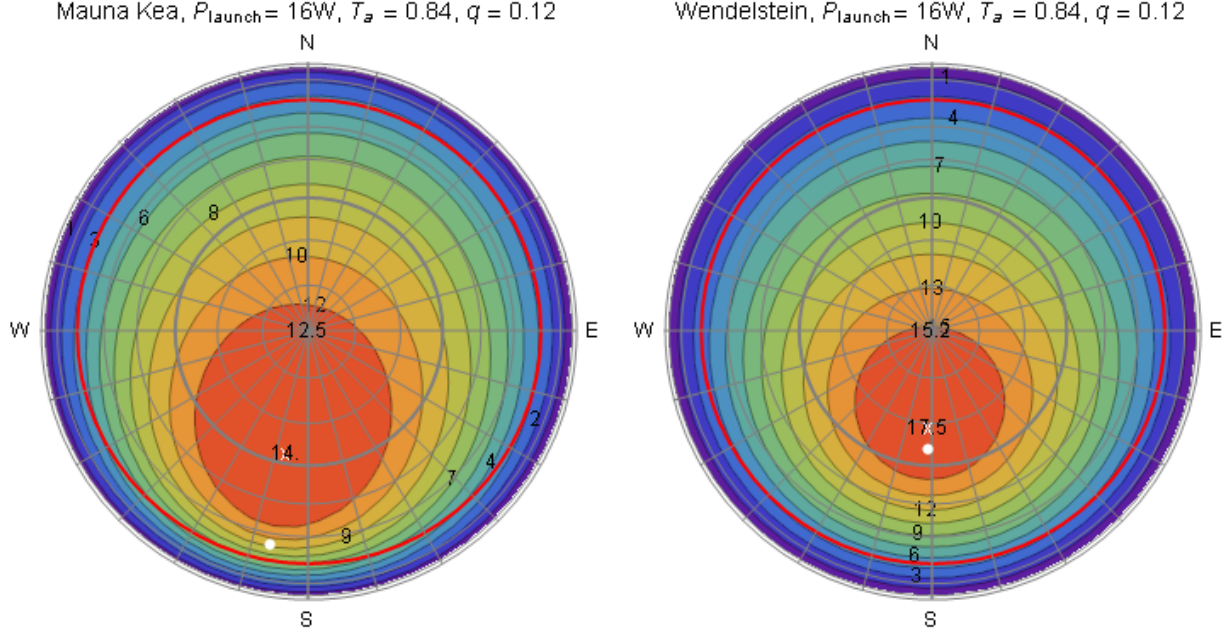
Fig. 7: Sky plots of Φ in 10^6 ph/s/m^2, Left: Mauna Kea, right: Mount Wendelstein, Germany (both 16 W in air, q = 12%).

4. SUMMARY AND CONCLUSIONS

In this work, we employ high-resolution LIDAR sodium density profiles that have recently become available [5]. Moreover, we simulate the laser mesospheric irradiance distribution using physical optics [2], depending on beam quality, laser projection equipment, and the atmospheric turbulence. We use a novel collision model for the sodium atoms. Finally, we compute the return flux efficiency depending on all of these inputs using optical Bloch equations [1] and integrate along the laser beam in the mesosphere. We are thus able to produce accurate sky maps of the photon return, depending on airmass and angle to the geomagnetic field.

We find that the return flux at 60° zenith angle reaches less than 1/3 of the flux at zenith. This strong decay is caused, besides simple geometry, by increasing light depletion in the sodium layer and by variable efficiency of optically pumping the sodium. The return flux distribution depends most strongly on two parameters: a) The local direction and magnitude of the geomagnetic field, b) laser power, polarization, and whether we apply D_{2b} repumping. By contrast, seasonal and diurnal variations in the mesospheric gas density and temperature profiles, as well as sodium distribution, play less of a role. It has to be further kept in mind that the return flux is essentially proportional to the sodium column density, which can vary strongly as a function of space and time. Since the average seasonal sodium column density depends on latitude, and because of the variation of the geomagnetic field with location, LGS laser power requirements may be different for different telescope sites, even for the same instruments. Ultimately, careful sky measurements of realistic 20+-watt class LGS systems are required to validate these simulations, and our team is building the necessary setup toward this goal.

Modern 20W-class LGS lasers with diffraction-limited beams will achieve good optical pumping, implying a nonlinear dependence of sodium excitation on laser irradiance. Such lasers hence must be defocused when accurate LIDAR profiles or column density measurements are desired.

Looking further ahead, we have modeled a laser with 360 W (in air), which may be a relevant peak power of future pulsed lasers for spot tracking. We find that we can retain about 85% of the efficiency in return flux per watt if the laser bandwidth is increased to a few tens of MHz.

REFERENCES

[1] Holzlöhner, R., Rochester, S. M., Bonaccini Calia, D., Budker, D., Higbie, J. M. and Hackenberg, W., "Optimization of cw sodium laser guide star efficiency", Astron. & Astrophys. **510**, A20 (2010)

[2] Holzlöhner, R., Bonaccini Calia, D. and Hackenberg, W., "Physical Optics Modeling and Optimization of Laser Guide Star Propagation", Proc. SPIE **7015**, pp. 701521–701521-11 (2008)

[3] Fried, D.L., "Optical resolution through a randomly inhomogeneous medium for very long and very short exposures", J. Opt. Soc. Am. **56**, pp.1372 (1966)

[4] Chang, F. C., Mott, H., and Webb, W.E., "Depolarization of an Uncollimated Laser Beam in a Turbulent Medium", J. of the Franklin Inst. **296**, pp. 347–358 (1973)

[5] Pfrommer, T., P. Hickson, and C.-Y. She, "A large-aperture sodium fluorescence LIDAR with very high resolution for mesopause dynamics and adaptive optics studies", Geophys. Res. Lett. **36**, L15831, doi:10.1029/2009GL038802, (2009)

[6] Moussaoui, N. , Clemesha, B. R., Holzlöhner, R., Simonich, D. M., Bonaccini Calia, D., Hackenberg, W., and Batista, P. P., "Statistics of the sodium layer parameters at low geographic latitude and its impact on adaptive-optics sodium laser guide star characteristics", Astron. & Astrophys. **511**, A31 (2010)

[7] Drummond, J., Novotny, S., Denman, C., Hillman, P., Telle, J., "The Sodium LGS Brightness Model over the SOR", AMOS 2007 Conference, pp. E67 (2007)

[8] Xiong, H., Gardner, C.S., and Liu, A.Z., "Seasonal and nocturnal variations of the mesospheric sodium layer at Starfire Optical Range, New Mexico", Chin. J. of Geophys. **46**, pp. 432–437 (2003)

[9] Drummond, J., "2006 Summary of 50 W Fasor Sky Tests and Model Summary", Version Feb 27, 2007, internal SOR report

[10] Moussaoui, N., Holzlöhner, R., Hackenberg, W. and Bonaccini Calia, D., "Dependence of sodium laser guide star photon return on the geomagnetic field", Astron. & Astrophys. **501**, 793–799 (2009)